Marine Pollution Bulletin 130 (2018) 40–54

Contents lists available at ScienceDirect

Marine Pollution Bulletin

journal homepage: www.elsevier.com/locate/marpolbul

Residual effects of treated effluent diversion on a seaweed farm in a tidal strait using a multi-nested high-resolution 3-D circulation-dispersal model

Yusuke Uchiyama[a,b,*], Xu Zhang[a], Yota Suzue[a,1], Taichi Kosako[b], Yasumasa Miyazawa[c], Akihiko Nakayama[d]

[a] Department of Civil Engineering, Kobe University, Kobe, Japan
[b] Coastal and Estuarine Environmental Department, Port and Airport Research Institute, Yokosuka, Japan
[c] Application Laboratory, Japan Agency for Marine-Earth Science and Technology, Yokohama, Japan
[d] Department of Environmental Engineering, Universiti Tunku Abdul Rahman, Kampar, Perak, Malaysia

ARTICLE INFO

Keywords:
Treated sewage effluent
Coastal dispersal
Diversion
Tidal strait
Estuary
ROMS

ABSTRACT

A high-resolution 3-D model was developed to assess the impact of a diversion outfall at the Tarumi Sewage Treatment Plant (TSTP) on an adjacent seaweed farm in Osaka Bay, Japan. The model was extensively validated to ensure a reasonable agreement with in situ observations. The western part of the farm is largely influenced by tidal currents, whereas the eastern area is mainly affected by subtidal residual currents that are primarily due to surface wind stress. The released effluent is transported by counterclockwise residual circulation formed off the TSTP. The model reveals that the diversion adequately suppresses the influence on the farm. While the instantaneous effluent concentration is diminished by about 50%, the effluent accumulated on the farm decreased from $2.83 \times 10^4\,m^3$ to $2.01 \times 10^4\,m^3$ due to the diversion, demonstrating an approximately 28% reduction of the effluent from the TSTP by the diversion outfall.

1. Introduction

The Seto Inland Sea (SIS) is the largest semi-enclosed estuary in Japan, encompassing a total water area of 23,203 km^2 (Fig. 1a). It has unique geographical characteristics and consists of seven main sub-basins interconnected by narrow straits and > 3000 islands, which form a complex "basin–strait" system. The SIS is a partially stratified tidal estuary that is concurrently affected by: 1) energetic tidal currents up to 3 ms^{-1} near straits (Fujiwara et al., 1994) under dominant semidiurnal, mesotidal conditions with a maximum tidal range of ± 1.2 m; 2) seasonally varying freshwater discharge from 28 major rivers; and 3) quasi-persistent eastward residual circulation (the SIS through-flow) primarily driven by the eastward drifting Kuroshio offshore of the two openings that connect the SIS with the Pacific (e.g., Kosako et al., 2016). The Kuroshio is known to have a considerable impact on the SIS circulation due to sporadic intrusions (Takeoka et al., 1993; Tada et al., 2017) and meandering of the Kuroshio path (e.g., Kawabe, 1987, 1995). In such a strait–basin system, the water is well mixed near straits due to strong tidal currents, while it is rather stratified in basins under more quiescent conditions (e.g., Guo et al., 2004; Chang et al., 2009).

Approximately 24% of Japan's population resides within its watershed basins (Tsuge and Washida, 2003), which leads to heavy nutrient loading of the SIS (Miller et al., 2010) and thus an increased occurrence of harmful algal bloom (HABs; e.g., Imai et al., 2006). Historically, the SIS has been extensively used by fisheries and in aquaculture, although it is viewed as a general dumpsite for wastewater from sewage treatment plants. This has caused the critical deterioration of the water quality and coastal marine ecosystems for many years (Tsujimoto et al., 2006). The number of "red tide" events due to HAB, an indicator of eutrophication, has raised remarkably with the increased nutrient loading (Takeoka, 2002; Imai et al., 2006). Red tides have occurred much more frequently and in a larger area in the SIS since the 1960s due to Japan's economic development and the associated pollutant emission, with the maximum of 299 incidents in 1976 (Imai et al., 2006). The aquaculture and marine ecosystem have been seriously affected by deterioration. Terawaki et al. (2003) reported that ~6400 ha of seaweed and seagrass beds along the Japanese coast have been destroyed from 1978 to 1991. A series of environmental preservation policies that regulate the total amount of nitrogen and phosphorus in effluent has been enacted, which had adequately improved the water quality in recent years (Tomita et al., 2016). However, deterioration is not entirely avoidable; ~100 red tides have occurred

* Corresponding author at: Department of Civil Engineering, Kobe University, Kobe, Japan.
E-mail address: uchiyama@harbor.kobe-u.ac.jp (Y. Uchiyama).
[1] Present affiliation: CTI Engineering Co., Ltd., Nagoya, Japan.

https://doi.org/10.1016/j.marpolbul.2018.03.007
Received 28 December 2017; Received in revised form 3 March 2018; Accepted 5 March 2018

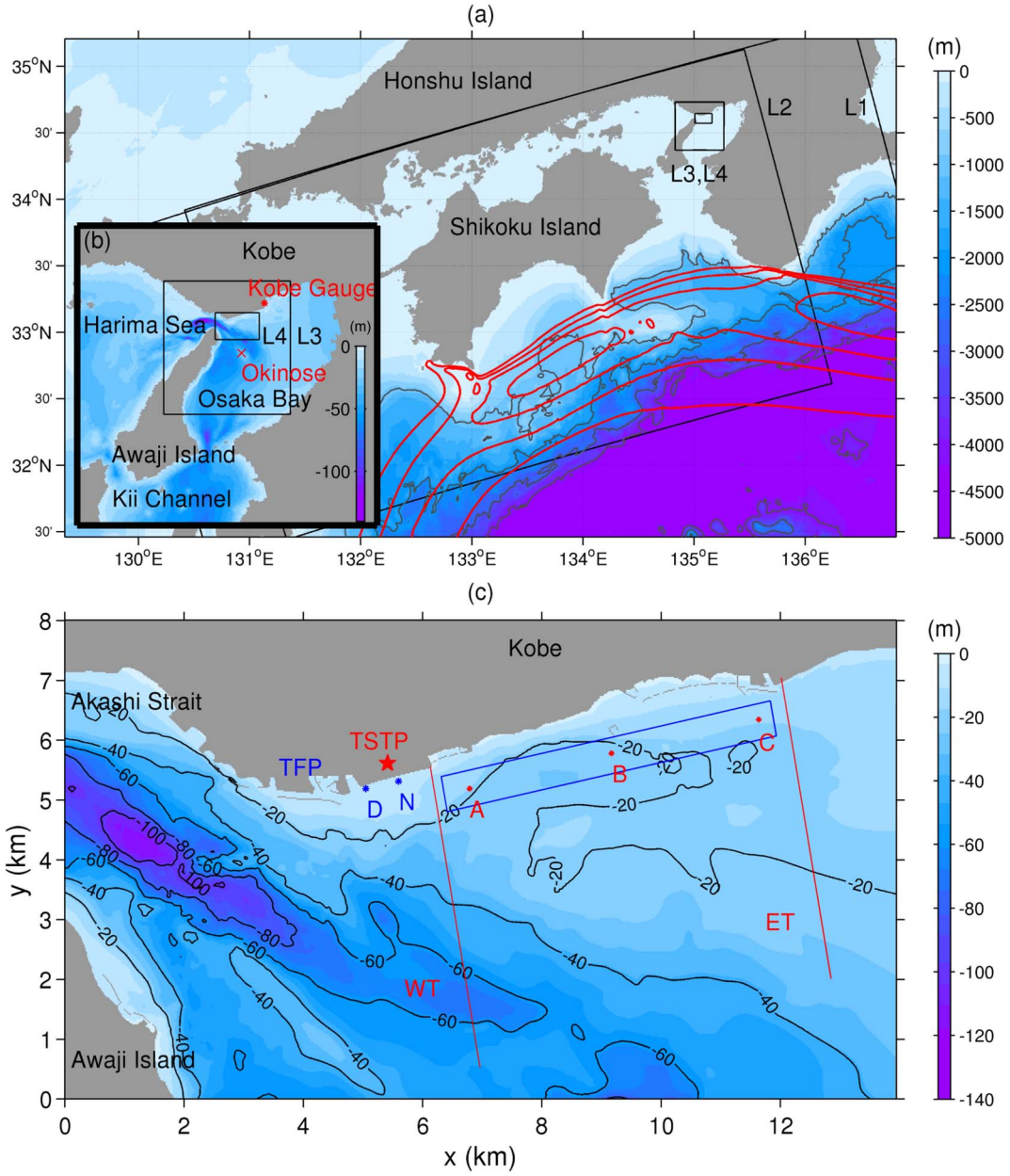

Fig. 1. Quadruple-nested ROMS model domains and bathymetry (color: m). (a) The ROMS-L1, L2, L3, and L4 domains (black boxes) embedded in the JCOPE2 domain (outside of the perimeter of the L1). The gray contours are the isobaths at intervals of 1000 m, while the red contours indicate the approximate Kuroshio region with surface velocity magnitudes ≥ 0.5 m/s at intervals of 0.25 m/s. (b) The enlarged area around Osaka Bay encompassing the L3 and L4 domains. The red dot and cross indicate the locations of the Kobe tidal gauge and shallowest part of the "Okinose" shoal at a depth of 23 m. (c) The entire L4 domain with isobaths at intervals of 20 m. The blue box is the approximate extent of the seaweed farm area; TFP is the Tarumi Fishery Port area; the red star shows the location of the Tarumi Sewage Treatment Plant (TSTP); the blue dots are the two outfalls (D: diversion, N: normal); the red dots (Stations A-C) are used for the time series plots in Figs. 5, 6, 7 and 11; and the red lines are two transects used for the cross-sectional plots of Figs. 9 and 10. (For interpretation of the references to color in this figure legend, the reader is referred to the web version of this article.)

per year in the SIS since the 2000s. Osaka Bay, located in the eastern part (Fig. 1b) with the most densely populated hinterland around the SIS, still suffers from severe water pollution.

The Tarumi Sewage Treatment Plant (TSTP), one of the largest wastewater treatment plants in Osaka Bay, is situated in the 3.6 km narrow Akashi Strait with a maximum depth of 140 m (Fig. 1c) and prevailing energetic and complex tidal flow. A sandbank known as the "Okinose" shoal (Fig. 1b) with the shallowest depth of 23 m is formed southeast of the strait, influenced by intense tidal currents and residual clockwise circulation (Fujiwara and Nakata, 1991; Fujiwara et al., 1994). The area around the Akashi Strait is famous for seaweed farming in the nation. Edible seaweed ("nori" in Japanese) is very common in Asia, which is made from a type of red algae, *Porphyra*, including widely cultivated *Porphyra yezoensis* and *Porphyra tenera* (Niwa and Aguga, 2006). Local fishermen keep complaining about the possible impact from sewage effluent on seaweed farming to the east of the TSTP (blue box in Fig. 1c). In seaweed farming, spores are rather vulnerable to the surrounding environment, in particular to nutrients and salinity. They grow rapidly from December to March and are harvested in April. Therefore, to avoid overdose that stunts seaweeds, a reduction of nutrients in the effluent is inevitable in fall. The City of Kobe, the local government, has constructed a new western diversion outfall ("D" in Fig. 1c) 500 m away from the central normal outfall ("N" in Fig. 1c) in the TSTP to reduce the possible impact of the effluent on farming by seasonal diversion from October to December. However, the effects of the western diversion have not been fully investigated, particularly in

comparison to the case with effluent from the normal outfall.

Bricker et al. (2006) described the general behavior of wastewater released from the western outfall of the TSTP based on conductivity, temperature, and depth (CTD) field measurements for one M_2 tidal cycle under mixed influences from riverine water from the adjacent small stream (Fukuda River). Bricker and Nakayama (2007; hereinafter BN07) further diagnosed the sewage effluent transport and diffusion from dilution quantified based on the filtered temperature and salinity fields that enable the separation of wastewater from ambient seawater influenced by the stream. Although both studies were conducted over a short duration under well-mixed winter conditions without any consideration of the normal outfall, the far-field freshwater plume behaves like those in a canonical open channel flow with respect to the vertical mixing, while horizontal mixing occurs with a diffusivity two (one) orders of magnitude larger than that of meandering (straight) channel flows. They anticipated that the estimated large lateral diffusivity may be due to topographically generated eddies, transient tidal flow, and baroclinicity in the buoyant plume. In contrast, multi-nested high-resolution numerical ocean modeling is useful to examine the far-field dispersal of effluent under such complex dynamical conditions. Uchiyama et al. (2014) comprehensively assessed the effects of diversion and dispersal of effluent with a quadruple-nested ocean circulation model coupled with a buoyant plume and passive Eulerian tracer in an open ocean configuration for Southern California bays. They found that lateral mixing and the associated effluent dispersal predominantly occur with submesoscale turbulence rather than tidal mixing.

In the present study, we conducted multi-nested, high-resolution, synoptic ocean circulation modeling to assess the dilution and far-field dispersal of the bottom-released buoyant effluent discharged from the central and western outfalls corresponding to normal and diversion discharges at the TSTP. The extrinsic effects of large-scale oceanic information, including the transient Kuroshio that determines the residual, eastward SIS throughflow, and the intrinsic variability, such as the fluctuating tidal flow and associated 3-D mixing, were thoroughly considered. We primarily aimed to examine possible driving mechanisms of the flow field near the TSTP and to quantify the impact of the diversion of sewage effluent on the seaweed farm. The remainder of the present paper is organized as follows. The configuration of the numerical model is given in Section 2. Section 3 illustrates and validates the model results followed by a discussion of possible driving mechanisms of the near-surface and 3-D flow fields around the TSTP in Section 4. A quantitative assessment of influences of the TSTP on the seaweed farm for cases with normal and diversion outfalls is conducted with a flux budget analysis in Section 5. The conclusions are provided in Section 6.

2. The nested model

2.1. The ocean circulation model

We developed a quadruple-nested downscaling ocean model (hereinafter L1–L4 models; Table 1 and Fig. 1) based on the Regional Oceanic Modeling System (ROMS; Shchepetkin and McWilliams, 2005, 2008) coupled with an Eulerian passive tracer model (Section 2.2) proposed in Uchiyama et al. (2014), which enables us to keep track of the effluent conservatively. The outermost boundary conditions for the ROMS models were imposed from the assimilative Japan Coastal Ocean Predictability Experiments (JCOPE2) oceanic reanalysis (Miyazawa et al., 2009) at the perimeter of the L1 model, as described in Uchiyama et al. (2017a, 2017b). Subsequently, the one-way offline nesting technique was used to successively convey large-scale information into the embedded child models with gradual grid resolution refinement (e.g., Mason et al., 2010; Buijsman et al., 2012; Romero et al., 2013; Kamidaira et al., 2017). The lateral grid spacing was thus reduced from 1/12° (~10 km, JCOPE2) to 2 km (L1), 600 m (L2), 100 m (L3), and 20 m (L4). The surface- and bottom-following, vertically stretched *s*-coordinate (Shchepetkin and McWilliams, 2005) with 32 *s*-layers was used for all four ROMS models with grid height refinement near the surface and bottom to resolve the boundary layers adequately. The bathymetry for the L1 and L2 models was provided by the SRTM30_PLUS product (Rodriguez et al., 2005; Rodriguez et al., 2006; Becker et al., 2009), which covers the global ocean at 30 geographic arc seconds (~1 km), supplemented by the J-EGG500 (http://www.jodc.go.jp/data_set/jodc/jegg_intro.html) at 500 m resolution for the coastal region. The bathymetry for the L3 and L4 models was obtained from the dataset compiled by the Central Disaster Prevention Council, Japan, with a horizontal resolution of 50 m.

The surface momentum flux (viz., wind stress) was taken from the hourly operational atmospheric product of the Grid-Point Values–MesoScale Model (GPV–MSM; Isoguchi et al., 2010) of the Japan Meteorological Agency (JMA). The surface heat and freshwater fluxes for L1 and L2 were obtained using the bulk formula that has been implemented in the Coupled Ocean/Atmosphere Mesoscale Prediction System (COAMPS; Hodur, 1997), while the surface fluxes for L3 and L4 were taken from the monthly climatology of the Comprehensive Ocean-Atmosphere DataSet (COADS; Woodruff et al., 1987) with the flux correction described in Uchiyama et al. (2017a). The principal ten tidal constituents from the TPXO7.0 global reanalysis (Egbert et al., 1994; Egbert and Erofeeva, 2002) were imposed as additional surface elevations along the perimeter of the L2 model. The freshwater discharge from all major rivers in each model domain is given as monthly climatological freshwater mass point source inputs based on the Annual Record of Rainfall and Discharge Database issued by the Japan River Association (http://www.japanriver.or.jp/publish/book/nenpyou_dvd.htm). Wave-driven currents (e.g., Uchiyama et al., 2010, 2017c) were omitted because of limited fetch effects that significantly diminish the

Table 1
Model configurations.

Models	L1	L2	L3	L4
Computational period	3/1/2006–11/31/2015	9/1/2006–11/9/2015	9/1/2015–11/9/2015	9/21/2015–11/9/2015
Grid cells	320 × 320 (×32 layers)	800 × 480 (×32 layers)	400 × 400 (×32 layers)	696 × 400 (×32 layers)
Horizontal grid resolution	2 km	600 m	100 m	20 m
Baroclinic time step	120 s	30 s	8.0 s	1.0 s (diversion); 1.5 s (normal)
Surface wind stress	JMA-MSM (hourly)	JMA-MSM (hourly)	JMA-MSM (hourly)	JMA-MSM (hourly)
Surface flux	COAMPS bulk formula	COAMPS bulk formula	COADS (monthly climatology)	COADS (monthly climatology)
Boundary/initial condition	JCOPE2 (daily)	ROMS-L1 (daily)	ROMS-L2 (hourly)	ROMS-L3 (hourly)
T-S nudging	JCOPE2 (10-day averaged)	None	None	None
Topography	SRTM30 + JEGG500	SRTM30 + JEGG500	CDPC	CDPC

CDPC: Central Disaster Prevention Council, Japan (50 m resolution).

wind waves and swells in the SIS. The innermost L4 model encompasses the TSTP and whole seaweed farm area (Fig. 1c) at a 20 m horizontal grid spacing, which sufficiently represents the complex bathymetry and horizontal topography including coastal structures. Treated freshwater discharge from the TSTP is also considered based on the measured data (City of Kobe, unpublished data).

Because seaweed spores are vulnerable to environmental stresses when they are sown on the farm in fall, we focused on boreal fall conditions from September to November when diversion occurs. The L4 model was run for ~50 days to include the whole month of October 2015 when the sewage effluent is most influential to the seaweed farm. Table 1 summarizes the numerical configuration of the L1–L4 models.

2.2. Sewage effluent model

Sewage effluent from diffusers at the sea bottom immediately rises and advects as buoyant plume. While releasing from diffusers and reaching the sea surface, the effluent also mixes with ambient seawater, which is called near-field dilution. Subsequently, far-field dilution takes over due to advection and diffusion by background currents. Because ROMS relies on a hydrostatic assumption and the L4 model still underresolves the detailed design of diffusers, it is inappropriate to explicitly model the near-field dilution, which is accompanied by intense buoyancy-driven vertical convective transport. Therefore, we made use of the near-field dilution model proposed by Uchiyama et al. (2014) embedded in the 3-D transport equation of the buoyant effluent, which is explicitly applicable to far-field behavior. A submodel for buoyant sewage effluent was implemented in the L4 model as an additional 3-D advection–diffusion model for an arbitrary conservative Eulerian passive tracer, in which the near-field dilution is modeled as an arbitrary source term $\mathscr{P}$:

$$\frac{\partial c}{\partial t} + \nabla \bullet \mathbf{u}c = \mathscr{D} + \mathscr{P}, \tag{1}$$

where c is the pollutant concentration normalized by C_p, $\mathbf{u}$ is the 3-D velocity of the ambient flow, $\mathscr{D}$ is the diffusion term, ∇ is the 3-D gradient operator, and C_p [kg m^{-3}] is the input pollutant concentration at the outfall. The underresolved nondimensional tracer source function $\mathscr{P}$ [s^{-1}] may be represented as follows:

$$\mathscr{P}(x,y,z;t) = P_s(t)A(x,y)H(z), \tag{2}$$

where P_s is the normalized tracer flux from the diffusers and A and H are the prescribed spatial shape functions of the plume above the outfall diffusers. The values of A and H are nondimensional, that is, close to one in the source region and zero outside of it. They were also utilized to resolve the spatial distribution in the source region. The associated spatial integral relations are:

$$\iint A\, dx\, dy = A_s, \int H\, dz = H_s, \tag{3}$$

where A_s is the horizontal area, H_s is the vertical size, and $V_s = A_s H_s$ is the volume of the prescribed plume. Hence, $P_s(t) = Q_p(t)/V_s$, where $Q_p(t)$ [m^3 s^{-1}] is the volume flux. Because the variable c is a nondimensional concentration, one can retrieve any arbitrary conservative concentration, such as colored dissolved organic matter (CDOM), nitrate, and ammonium, by multiplication with a factor C_p, which corresponds to the mean concentration at the point source. Note that a similar source term was added to the 3-D mass, momentum, salinity, and temperature conservation equations to account for near-field dilution effects.

The shape functions A and H were also described according to Uchiyama et al. (2014). We assumed that the peak of the released sewage flux occurs at the sea surface with downward exponential decay following a Gaussian distribution:

$$H(z) = \exp\left[-\frac{(z - z_s)^2}{d_s^2}\right], \tag{4}$$

where z_s is the plume center height and d_s is the vertical scale of the plume. For our outfall design, z_s was set to be 0 m for the surface-confined shape with d_s of 7 m, the local mean depth. The sewage effluent was applied at the locations of the two outfalls (normal and diversion) as bottom-released freshwater plume at a constant volume rate of 1.80×10^5 m^3 d^{-1}. The discharged nondimensional passive tracer was always set to unity (one) with the temperature of the ambient seawater (i.e., no net heat supply) and zero salinity. The diversion and normal outfalls are represented by two and four grid points, respectively (viz., footprint of 20 m × 40 m for the diversion and 20 m × 80 m for the normal outfall). Their centers are located 80 m and 40 m offshore from the sea wall of the TSTP, which approximately corresponds to the pipe lengths of the central (normal) and western (diversion) outfalls, respectively.

It is worth mentioning that a more elaborate near-field mixing model could be alternatively used for the source term $\mathscr{P}$ in order to reflect realistic behavior of a transient buoyancy plume at the outfall pipes. A possible direction is to employ a sophisticated 3-D near-field model such as the one based on a non-hydrostatic LES model (Nakayama and Nizamani, 2016). Such an implementation into the present system is viable, and should be conducted in future work.

3. Model validation

3.1. Hydrodynamics

The newly developed L3 and L4 models were validated with observed data. The parent L1 and L2 models agree well with in situ measurements of temperature, salinity, and tides for the 9-year period from 2006 to 2015 in Kosako et al. (2016). Fig. 2 shows scatter plots of the modeled and measured sea surface temperature (SST) and salinity (SSS). The observed data are based on repeated CTD measurements from vessels and are available as a part of "The Comprehensive Water Quality Survey in the Seto Inland Sea" collected and maintained by the Ministry of Land Infrastructure and Transport, Japan (http://www.pa.cgr.mlit.go.jp/chiki/suishitu/). The areas outside of the L3 and L4 domains are supplemented by the L2 result. The model shows an outstanding SST reproducibility (Figs. 2a and 3), whereas it is moderate for SSS with a correlation coefficient of 0.379 (Fig. 2b). Such an overall reasonable reproducibility is inherited from their parent models (Kosako et al., 2016). The modeled SSS is overestimated because our model merely accounts for the monthly climatology of the major rivers (Section 2.1) that results in the underestimation of freshwater input to the SIS. Nevertheless, the estimated average density error of the surface layer caused by the erroneous freshwater input is only 0.14%, leading to subtle effects on the near-field submodel (Section 2.2) and the result presented below. The inclusion of temporally varying synoptic freshwater discharge from the rivers, hundreds of unnamed small streams, and groundwater seepage ubiquitous along the shoreline should improve the salinity reproducibility. Our implementation is apparently suboptimal; however, detailed freshwater data are not publicly available for the SIS. Kurosawa et al. (2017) supported this speculation based on the same L2 SIS model with data assimilation and indicated that heavy precipitation has a prominent influence on the river discharge in September and October, which appropriately corrects biases in the simulated SSS. Our choice is considered as the least bad option, which must be reconciled in future based on data availability.

We next verified the time-varying surface elevations mainly due to tides at the Kobe tide gauge station (Fig. 1b) operated by the JMA and maintained by the Japan Oceanographic Data Center (JODC; http://jdoss1.jodc.go.jp/vpage/tide_j.html). Tidal harmonic analysis was conducted with the modeled and measured hourly surface elevation, as summarized in Table 2, for four principal tidal constituents (M_2, S_2, K_1,

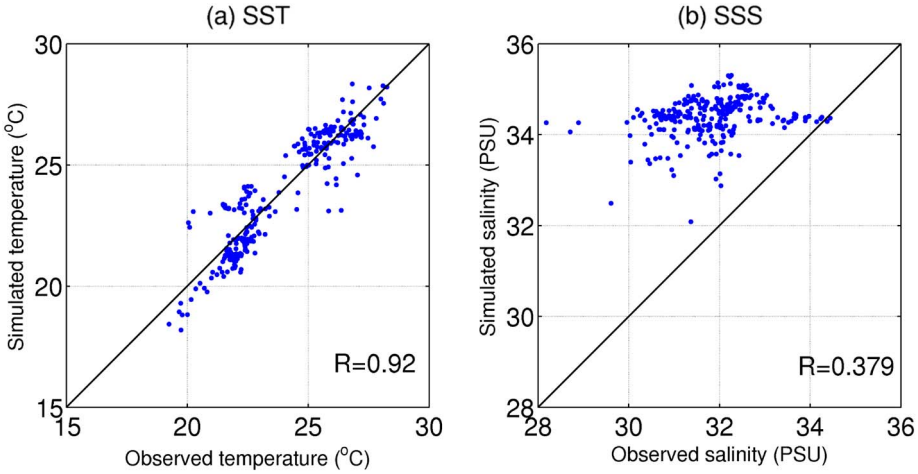

Fig. 2. Scatter plots of (a) SST (temperature) and (b) SSS (salinity) at the surface from discrete ship observation versus the corresponding model results. In each panel, R indicates the correlation coefficient between the model and observations.

and O_1). The tidal amplitudes and phases were reasonably well reproduced by the model, with correlation coefficients of 0.9785 and 0.9996, respectively. Slightly less agreement was obtained for the two semidiurnal constituents. These biases are already included in the TPXO7.0 that provides lateral boundary conditions for barotropic tides along the L2 perimeter (Section 2.1). The direct comparison of the elevations before applying the harmonic decomposition including winds and other subtidal variability yields a correlation coefficient of 0.887 (not shown). In general, the high-resolution L3 and L4 models exhibit a reasonable reproducibility of the mean and transient hydrodynamics around Osaka Bay, although there certainly is room for improvement. We leave these issues for future work.

Table 2
Result of the tidal harmonic analysis of the modeled (ROMS-L3) and observed (JMA) hourly surface elevation at the Kobe tidal gauge.

	Amplitude (m)			Phase (deg.)		
	OBS	MDL	DIF	OBS	MDL	DIF
M_2	0.3112	0.4216	−0.1104	307.8853	300.0558	7.8295
S_2	0.1846	0.2647	−0.0801	310.6101	304.0042	6.6059
K_1	0.1915	0.2345	−0.0430	53.9154	61.8425	−7.9271
O_1	0.1405	0.2116	−0.0711	47.0540	45.0413	2.0127

OBS: JMA observation data; MDL: ROMS-L3 model data;
DIF: Difference (observation - model).

3.2. Sewage effluent dispersal

The bulk behavior of the modeled sewage effluent was compared with the measured freshwater plume from the western diversion outfall of the TSTP (Fig. 1c). We chose to qualitatively compare it with the in situ measurement described in BN07, where an empirical, ad hoc filter was applied to the T–S diagram to separate the sewage effluent from ambient seawater and riverine freshwater. Vessel-based acoustic Doppler current profiler (ADCP) and tow-body CTD measurements were repeatedly conducted on December 1, 2005, ~3 days before the spring tide, for almost one M_2 tidal cycle (~10 h) in a narrow 1 km × 1 km region off the TSTP diversion outfall. Nevertheless, the signals of the freshwater effluent represented by the filtered salinity fraction were detected mostly in this 1 km × 1 km box and barely extended further in the offshore and alongshore directions. The most striking finding of BN07 (see their Fig. 4) is the asymmetric, alongshore-confined effluent transport due to prevailing alongshore currents constrained by the topography. During phases with slack to flood tides, westward alongshore currents developed inducing westward effluent transport toward the Akashi Strait, while the breakwater of the adjacent fishing port located in the west of the TSTP notably affected both of them to regulate southward offshore current and transport. As a result, the effluent mostly stayed within ~400 m from the outfall. Subsequently, an ebbing

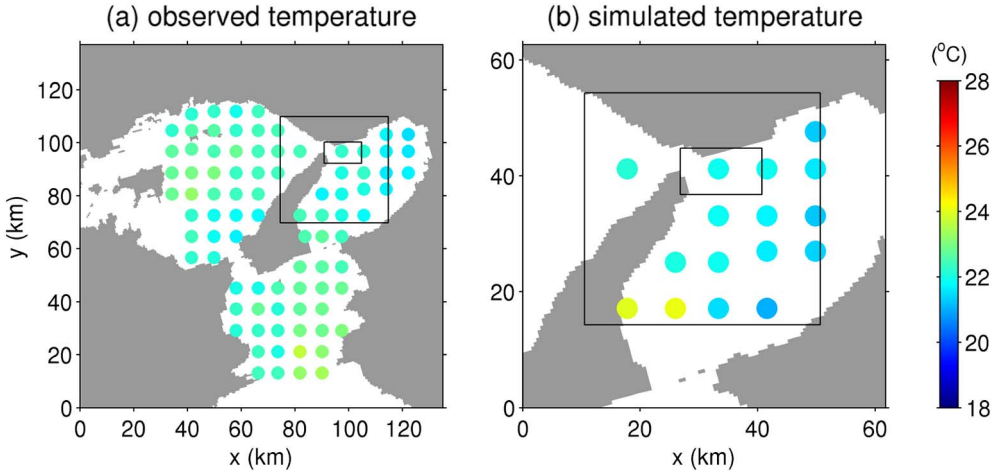

Fig. 3. Spatial maps of the (a) observed SST shown in Fig. 2 and (b) corresponding computed SST using the ROMS-L4. The black boxes are the L3 and L4 domains. Note that the observations were conducted by vessels for seven days in October 2015.

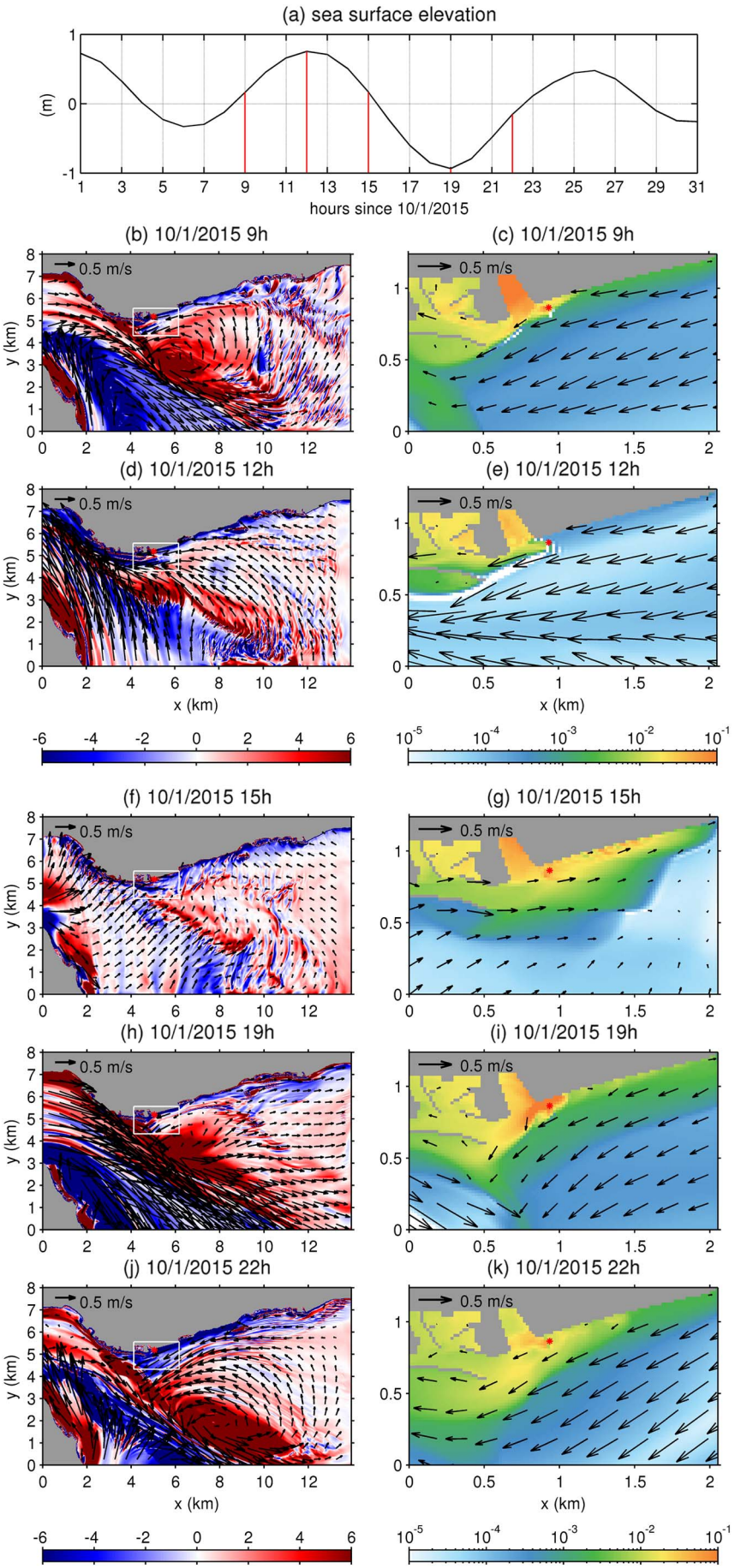

Fig. 4. (a) Time series plot of the sea surface elevation 1 km offshore of the TSTP starting at 1:00 UTC on October 1, 2015. The five red vertical lines indicate the selected surveys at 9:00, 12:00, 15:00, 19:00, and 22:00 UTC on October 1, 2015, as shown in the panels (b)–(k). Snapshots (hourly-averaged data) of the vertical component of relative vorticity (s^{-1}) at the surface normalized by the local Coriolis parameter (color) on the left during each survey at the indicated time. The right panels show the corresponding normalized passive tracer concentrations, c (color), in the enlarged area near the TSTP (white boxes in the left panels). The red dots represent the location of the western diversion outfall. The vectors are superposed to show the subsampled instantaneous surface velocity. The arrows in the top-left corner of each plot indicate the velocity scale of 0.5 m/s. (For interpretation of the references to color in this figure legend, the reader is referred to the web version of this article.)

phase manifested to promote shore-confined eastward currents and associated shore-trapped eastward effluent transport, followed by another flow reversal with a more prominent flood tide than the previous flooding. Interestingly, the shore-trapped effluent in the east of the outfall remained there for several hours, even at reverted westward offshore currents of the flooding tide. BN07 speculated that nearshore clockwise recirculation with the cross-shore extent of ~200 m formed to entrain the effluent within the overall westward current. Honda et al. (2007) extended the Eulerian analysis of BN07 by using Lagrangian surface drifters equipped with conductivity–temperature sensors, reassuring the alongshore asymmetric effluent dilution, where relatively stagnated, less diffusive eastward transport took place during an ebb, while more diffusive westward transport was provoked in conjunction with remote influence of intense offshore tidal currents generated in the Akashi Strait. Such a small-scale, coastally trapped dispersal of the buoyant effluent is solid evidence for the fact that we need high-resolution modeling with larger-scale ambient currents.

Fig. 4 shows the sea surface elevation in the top panel and sequential five pairs of snapshots of the relative vorticity (left panels) and corresponding normalized passive tracer concentration c in the enlarged area near the TSTP (right panels) at the surface with subsampled surface velocity vectors for the western diversion case on October 1, 2015. Because the prevailing westward currents formed during flood tide (Fig. 4b and c) and reach a maximum at the highest slack tide (Fig. 4d and e), the surface sewage released from bottom-mounted diffusers is also transported westward at the surface and confined near the shore (Fig. 4c and e). Subsequently, the currents weaken and change direction during ebb, resulting in eastward sewage transport (Fig. 4f and g). The wastewater distribution is largely affected by the fishing port just west of the TSTP during this period, in particular by its detached breakwater located ~150 m offshore to notably entrain a tracer in the port (Fig. 4g). Then, a flow reversal occurs at the lowest slack tide (Fig. 4h and i) retaining the eastward currents formed around the offshore deep channel of the strait, while westward flow is predominant in the nearshore shallow area. Such a cross-shore reversal of the alongshore flow direction results in the promotion of rather strong vorticity in the channel and near the coastline bend next to the TSTP (Fig. 4h). Counterclockwise circulation also forms around the eastern tip of the breakwater transporting the effluent offshore (Fig. 4i). Therefore, the tracer is widely distributed in the cross-shore direction at low tide. The sewage is transported westward during the flood due to the counterclockwise lateral circulation formed off the TSTP that promotes nearshore westward flow (Fig. 4j and k). In summary, the model successfully reproduces tidally-driven, asymmetric, alongshore-dominated, shore-trapped effluent dispersal patterns consistent with those observed in BN07; however, there are several minor discrepancies mainly due to different periods.

4. Dynamics

4.1. Surface currents

Spatiotemporally varying currents mainly driven by tides near narrow straits have been of great interest (e.g., Imasato, 1983; Imasato et al., 1994; Li et al., 2015). Our study area is in such a setup, where the narrow Akashi Strait repeatedly generates quite intense tidally driven currents that affect both the transient and residual dynamics and the resultant effluent dispersal near the TSTP (Section 3). Fig. 5 shows the surface residual velocity vectors as monthly averaged velocity with colors illustrating their magnitude and a time series plot of hourly surface velocity at Station A (Fig. 1c) for the diversion case. Strong tidal currents are repeatedly formed and intrude southeastward (northwestward) into Osaka Bay (Harima Sea) through the narrow Akashi Strait flanked by the Honshu and Awaji islands (Fig. 1b). Both the zonal (alongshore) and meridional (cross-shore) surface velocities considerably fluctuate at the semidiurnal period with a peak speed of 0.6 m/s and 0.2 m/s, respectively. Such a velocity variation is consistent with the ADCP measurement in the SIS (e.g., Kobayashi et al., 2009).

The residual currents have a complex distribution (Fig. 5a), primarily consisting of the 1) northwestward coastal current along the northeastern shore of Awaji Island; 2) clockwise circulation off Awaji Island and the TSTP, which is often referred to as the "Okinose Circulation" (e.g., Nakatsuji et al., 1994; Mishima et al., 1999), while only the northern part is depicted here; and 3) counterclockwise circulation off the TSTP, consistent with the model result in Imasato (1983). The velocity magnitudes of the three predominant currents are the largest. The coastal current along Awaji Island veers clockwise and points northeastward at $y \approx 5$ km. It then further turns clockwise to form the southeastward current that detaches from Honshu near the bend of the coastline at $x \approx 3$ km next to the TSTP and eventually merges with the Okinose Circulation. The counterclockwise circulation near the TSTP is accompanied by the westward nearshore current, which veers left to the offshore and then coalesces with the Okinose Circulation off the TSTP. Therefore, the surface currents mostly converge off the coastline bend near the TSTP. Fig. 4 shows that the effluent from the TSTP drifts westward near the shore after the release and turns offshore. Subsequently, it is entrained in the Okinose Circulation and transported southeastward toward Osaka Bay. Such a transport pattern is anticipated to reduce the direct impact of the effluent on the seaweed farm located in the east of the TSTP.

4.2. Underlying mechanisms

We carried out a spectral analysis to examine possible driving mechanisms of the flow field around the seaweed farm. Fig. 6 compares the frequency spectra of the surface currents $\mathbf{u}_s = (u_s, v_s)$, wind stress at 10 m above the sea surface $\boldsymbol{\tau}_s = (\tau_u, \tau_v)$, and surface elevation ζ at Station A (Fig. 1c) for October 2015. The variables u_s and τ_u represent the zonal (eastward) component, while v_s and τ_v reflect the meridional (northward) component. Two distinctive peaks commonly appear in both components at diurnal and semidiurnal frequencies of the surface velocity and ζ with moderate semidiurnal predominance. The wind stress spectra are "red" with low-frequency prevalence and no notable peaks, whereas the diurnal variability manifests modestly, presumably reflecting land–sea breeze cycles.

We further conducted a spectral coherence analysis among the variables (Fig. 7) at the three selected locations on the seaweed farm, i.e., Stations A–C, (Fig. 1c). The coherences of the alongshore velocity u_s against τ_u and ζ (left column) are distributed similarly at all three stations. The coherences are commonly high at diurnal and semidiurnal frequencies. However, the coherences between u_s and ζ are much higher (> 0.9) than those between u_s and τ_u (< 0.5), demonstrating that tidal currents dominate wind stresses and generate alongshore surface currents on the farm and thus the resultant effluent dispersal. In the higher subtidal frequency band at ~0.2–0.5 cpd, u_s is influenced by both tidal current and wind stress at Station A (Fig. 7a). In contrast, the coherence versus τ_u decreases gradually at Stations B and C when moving away from the TSTP (Fig. 7c and e), indicating that wind becomes less influential. In the frequency band much lower than 0.2 cpd, the lower subtidal ζ and low-frequency wind jointly affect the surface current at Station C with coherence by ~0.4, which in turn decreases at Stations A and B. Nevertheless, the coherence of the cross-shore velocity v_s (right column) substantially differs from that of u_s. Although the coherence between v_s and ζ is high at diurnal and semidiurnal frequencies near the TSTP (viz., Station A), it rapidly decreases when leaving the TSTP. The semidiurnal and diurnal coherence against wind stress is always low. In contrast, the subtidal coherence against ζ and τ_v for the band below 0.5 cpd, particularly 0.2–0.5 cpd, is much larger than that for u_s.

These results clearly indicate that tidal currents prevail near the TSTP, primarily provoking alongshore currents that are rectified by the

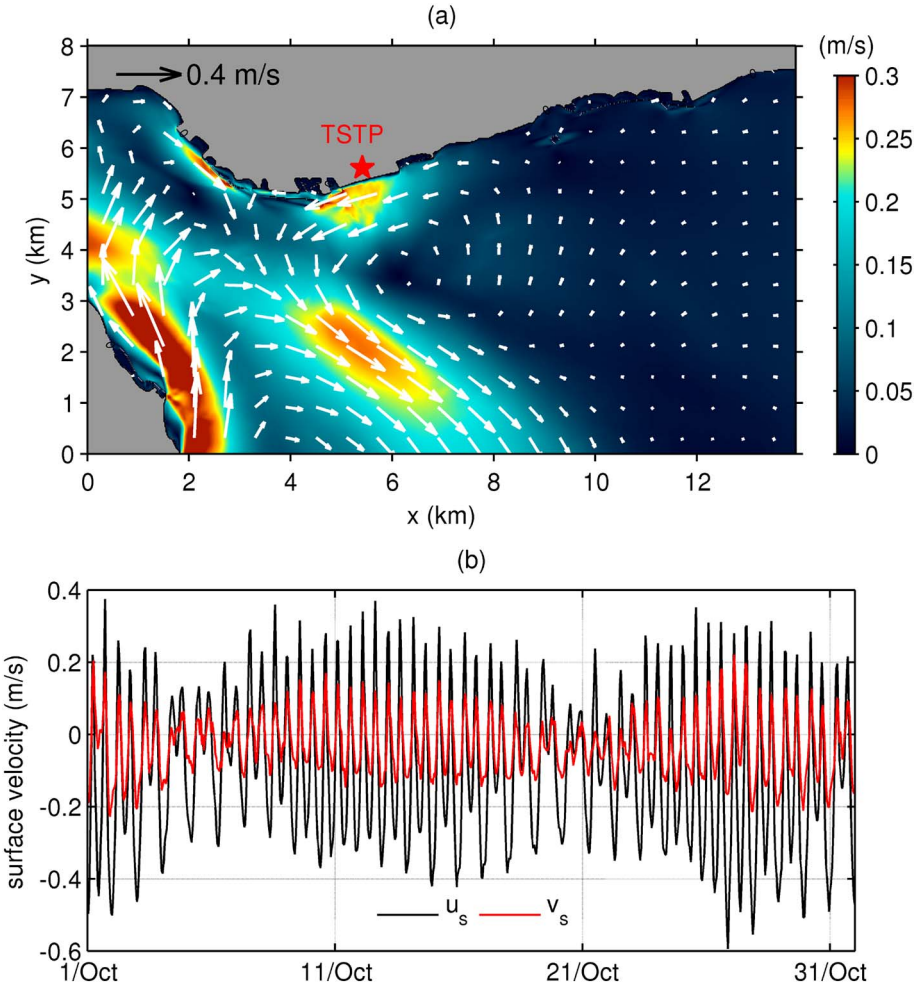

Fig. 5. (a) Monthly mean surface velocity vectors (white arrows) on their own magnitude (color). (b) Temporal variability of the eastward (u_s, black) and northward (v_s, red) surface currents at Station A (Fig. 1c) for the diversion case. (For interpretation of the references to color in this figure legend, the reader is referred to the web version of this article.)

coastline and topography, whereas such topographic constraint is relaxed at Station A, where the tidal ellipse is more circular (not shown). At locations distant from the Akashi Strait on the shallow shelf (Stations B and C), tidal currents are intensely constrained by topography and the cross-shore currents vary mostly depending on low-frequency wind and ζ. The low-frequency ζ variability is due to subinertial motions forced by the low-frequency wind variability. Eddies may play another important role. The seaweed farm experiences unique hydrodynamic conditions on a shallow shelf in the north of the deep channel, where the Okinose Circulation develops (Fig. 5a). The western part of the farm (viz., Station A) is controlled by tides and subtidal cross-shore currents. The central (Station B) and eastern (Station C) parts of the farm are in mixed configuration, where the alongshore currents are tidally driven, while the cross-shore currents are influenced by low-frequency wind, not by tides. In the subtidal frequency band lower than 0.2 cpd, the subtidal ζ solely contributes to cross-shore subtidal currents, reflecting much larger-scale flows including the quasi-persistent eastward SIS throughflow maintained by the transient Kuroshio (e.g., Kosako et al., 2016).

5. Impact of diversion

5.1. Time-averaged horizontal structures at the surface

Because seaweed growth relies on adequate light driving photosynthesis, the near-surface euphotic layer is most inhabitable for

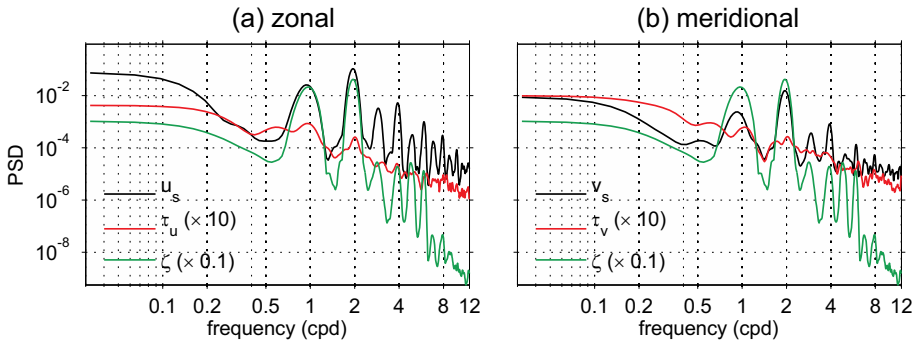

Fig. 6. Power spectral densities (PSDs) of the (a) eastward surface velocity, u_s, eastward wind stress, τ_u, and sea surface elevation, ζ, and the (b) northward surface velocity, v_s, northward wind stress, τ_v, and ζ at Station A (Fig. 1c). The units of the PSDs for velocity, wind stress, and elevation are (m^2/s^2)/cpd, (N^2/m^4)/cpd, and (m^2)/cpd, respectively, where cpd stands for cycles per day.

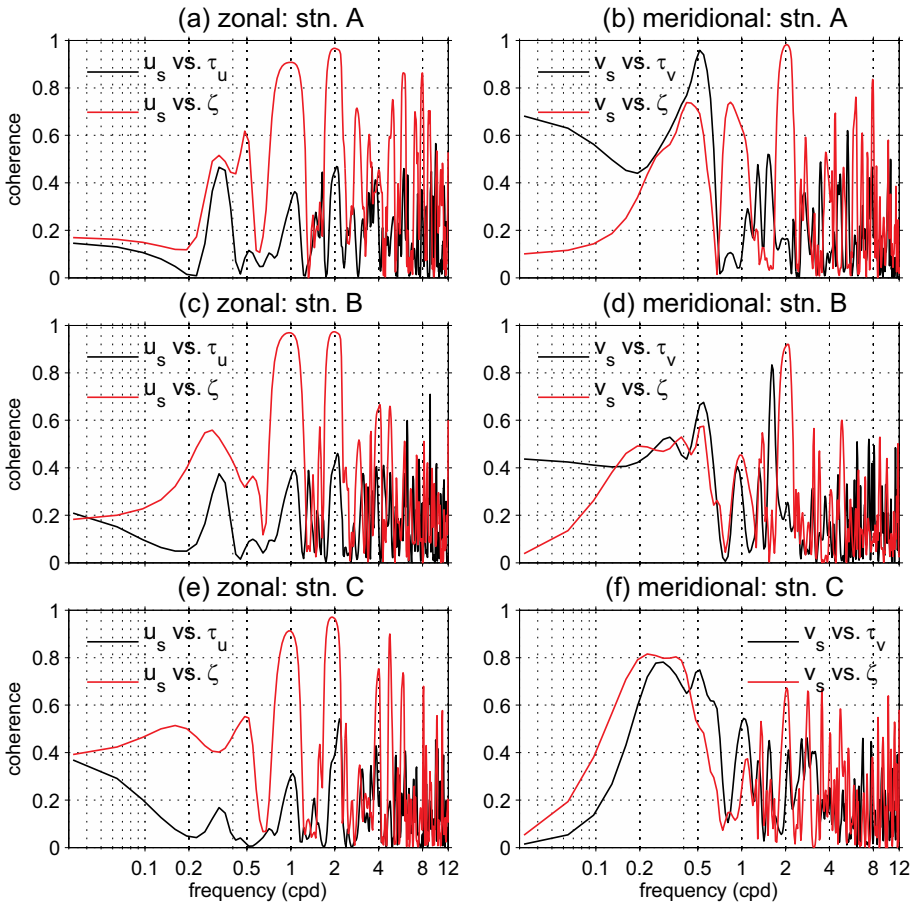

Fig. 7. Left: spectral coherences of u_s versus τ_u (black) and ζ (red); right: spectral coherences of v_s versus τ_v (black) and ζ (red) at Station A (panels a and b), Station B (c and d), and Station C (e and f). The locations of the three stations are shown in Fig. 1c. (For interpretation of the references to color in this figure legend, the reader is referred to the web version of this article.)

seaweeds (Abowei and Ezekiel, 2013). Therefore, surface effluent transport and its accumulation are the most essential factors to be assessed. Fig. 8 shows the monthly averaged SSS (contours) and passive tracer concentration c normalized by the source concentration C_p (Section 2.2) at the surface, representing effluent far-field dilution (color) averaged for the month of October 2015. The result for the case with diversion discharge from the western outfall is depicted in the top, while the differences (diversion case – normal case) are shown in the bottom. A weak lateral salinity gradient is formed with lower SSS in the northeast (Fig. 8a), primarily due to riverine freshwater discharge from major rivers in the inner Osaka Bay further east and influences from the buoyant plume of the freshwater effluent. The SSS difference between the two cases is nontrivial, with a factor of several percent relative to the spatial SSS difference (Fig. 8b). The western diversion results in an overall salinity increase near the coast including the eastern shore close to the seaweed farm, except for the area just off the TSTP, where freshening occurs approximately 3 km from the shore. A similar pattern is observed in the temperature field, although it is subtle with SST differences of no more than 0.01 °C (not shown). Hence, the effect of the locations of the outfall on buoyancy-driven dynamics is not significant.

The surface effluent dilution c is distributed similarly to SSS in the diversion case and is confined mostly near the shore on both zonal sides relative to the TSTP, with a pronounced eastward bias, in particular around the TSTP (Fig. 8a). In the eastern shallow area, c is widely extended offshore, with notable cross-shore dilution at depths below ~40 m (see Fig. 1c). This pattern is consistent with that of surface residual currents (Section 4), where strong currents are mostly formed in the deeper channel constrained by topography. The diversion significantly reduces the nearshore c (cold color), particularly near the shore including the majority of the seaweed farm area (white box in Fig. 8b). Similarly to SSS, the diversion increases c just offshore the TSTP (warm color) in an offshore extent of ~3 km. Such spatial differences in the effluent concentration and salinity are considered to be due to counterclockwise circulation formed off the TSTP as part of the Okinose Circulation, where westward currents that develop near the eastern shore transport the released tracers westward and then seaward off the TSTP and entrain in the circulation to promote eastward transport in the offshore area.

5.2. Time-averaged vertical structures

While our primary interest is the near-surface processes, vertical structures of the time-averaged c and salinity (S) are briefly discussed. We introduce two nearshore transects normal to the shore approximately defined at the western and eastern boundaries of the seaweed farm area, indicated by the red lines in Fig. 1c. Fig. 9 shows the cross-sectional plots of the monthly averaged c (color) and S (contours) along the western transect for October 2015 for the diversion case (Fig. 9a), difference between two cases (diversion – normal; Fig. 9b; denoted by ΔS and Δc), and corresponding enlarged plots for the nearshore area (Fig. 9c and d). The red contours in Fig. 9b and d represent the isohalines for $\Delta S = 0$ psu, while the solid and dotted white contours are the positive and negative values (intervals: 0.005 psu). The spatial distributions of c and S are largely consistent with each other (Fig. 9a), exhibiting that the buoyant effluent plume from the outfall transports increased c and decreased S simultaneously. The effluent plume is most considerable in the nearshore area, where S is lowered near the surface to form buoyantly stable stratification. Therefore, c is consistently distributed, mostly in the area in which freshening takes place. The diversion alters c and S only in a limited area (~1 km from the shore), with somewhat different spatial patterns (Fig. 9b and d). With the diversion, S increases near the surface due to the reduced freshwater

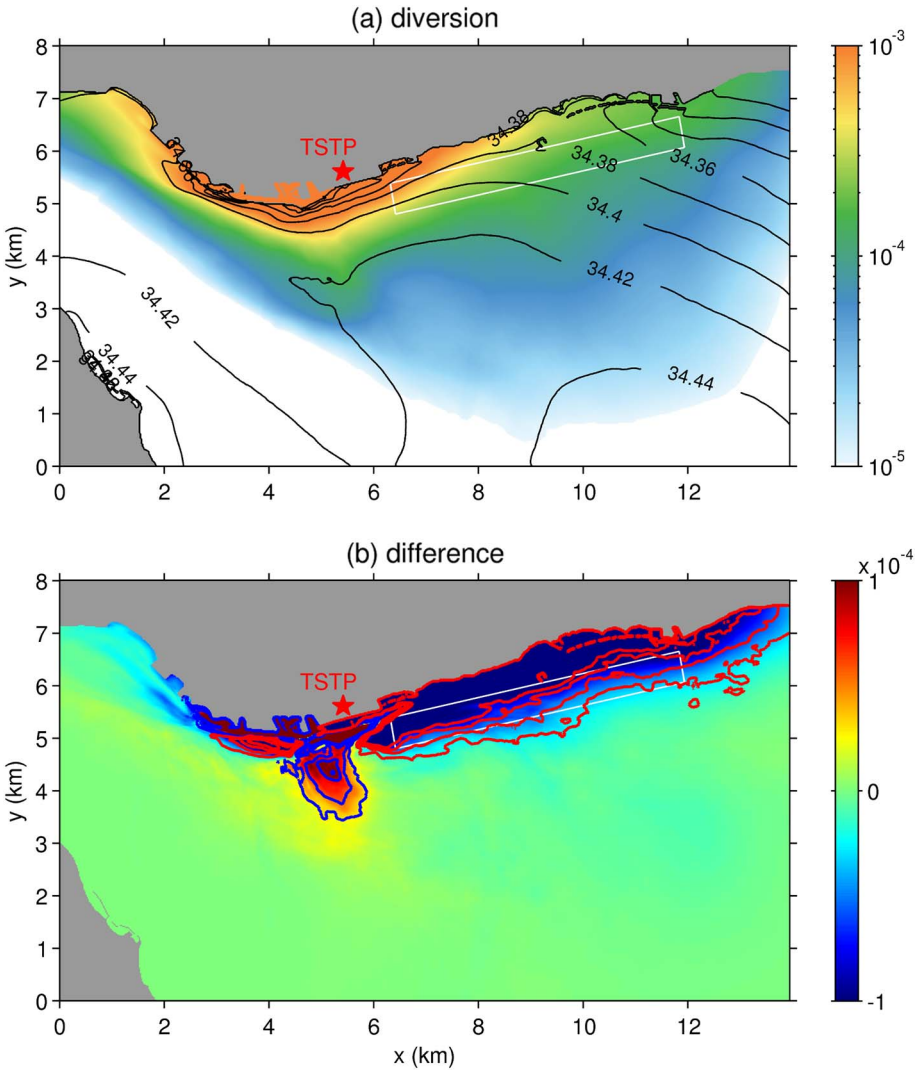

Fig. 8. (a) Monthly mean passive tracer concentration, c (color, nondimensional), at the surface for the diversion case. The black contours and labels denote the sea surface salinity (SSS; intervals: 0.02 psu). (b) The difference of c (color, nondimensional) and SSS (contours) between the two cases (diversion - normal). The red and blue contours are the positive and negative values (intervals: 0.001 psu), respectively. (For interpretation of the references to color in this figure legend, the reader is referred to the web version of this article.)

effects from the TSTP (solid white contours), while it decreases in the lower layer near the shore (dotted white contours). Likewise, the diversion generally decreases (increases) c when S increases (decreased). In particular, c is always diminished in the near-surface layer shallower than ~3 m depth with the diversion outfall, which reduces the influence of the effluent from the TSTP on the seaweed farm. However, the diversion lowers c in the shallow area within ~200 m from the shore, where S is enhanced (Fig. 9d). This minor difference in the cross-sectional spatial patterns of the deviations in c and S due to the diversion is most likely attributed to the river-originated fresher S source mainly from the east, which promotes more intense recurring westward effluent transport in front of the TSTP extending to the northwestern corner of the farm compared with that of c (Fig. 8b). On the other hand, the diversion results in an increase of the near-surface S to promote a vertical overturning circulation cell that entrains c in the middle of the cell and forms the positive subsurface Δc maximum.

Fig. 10 shows that the cross-sectional structures of c and S along the eastern transect (Fig. 1c) and their differences associated with the diversion are much simpler at smaller values than those along the western transect. In the diversion case (Fig. 10a), freshening due to the riverine water from the east is notable within ~2 km from the shore, as shown by the SSS in Fig. 8a. The offshore extent of the effluent c is approximately in the same range as that of S. The increase of S and decrease of c due to the diversion are more confined to the shore (~1 km to the sea), whereas the former is negligibly small. The surface-trapped diversion effects in Fig. 10b are not as evident as that observed along the western transect (Fig. 9b), supporting that the TSTP-originated buoyant plume is much less influential near the surface along the eastern transect. These results suggest that buoyancy effects due to freshwater effluent moderately alter the nearshore 3-D flow and associated c distribution, particularly near the TSTP.

5.3. Spatiotemporal variability

The effects of the sewage effluent from the two outfalls on the seaweed farm were examined using time series plots of the surface c (Fig. 11) at the three selected farm locations defined in Fig. 1c. The effluent concentration c gradually decreases from Stations A to C with increasing distance from the TSTP. Because the differences of the surface c at the three stations depicted by the green curves have apparent negative biases, the diversion outfall adequately reduces c in the farm. The temporal fluctuations of c for both the normal and diversion cases differ at the three stations. Although high-frequency tidal variability is observed at the westernmost Station A located ~1 km from the TSTP, much lower-frequency subtidal fluctuations are superposed on the tidal signals at the central Station B. Furthermore, at the easternmost Station

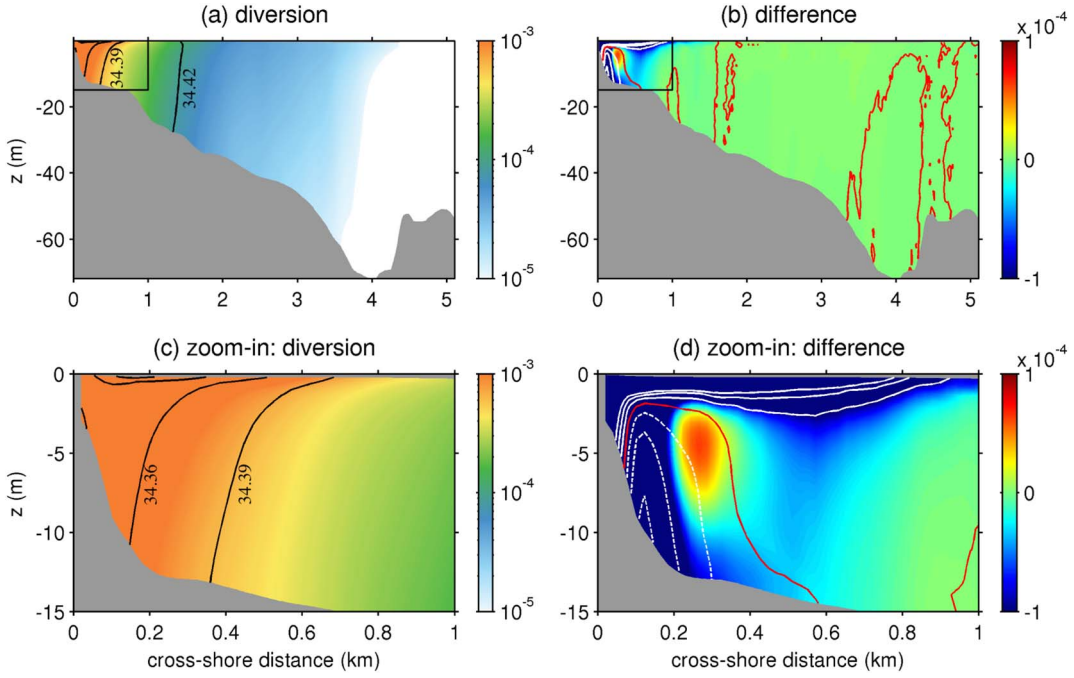

Fig. 9. (a) Cross-sectional plot of the monthly mean tracer concentration, c (color, nondimensional), at the western transect (WT in Fig. 1c) for the diversion case. The black contours and labels denote the salinity at intervals of 0.03 psu. (b) Cross-sectional plot of the difference of c (color, nondimensional) between the two cases (diversion - normal). The red contours represent zero, while the solid and dotted white contours are the positive and negative values at intervals of 0.005 psu, respectively. (c) and (d) show the enlarged nearshore areas depicted by the thin black boxes around the upper-left corners of (a) and (b), respectively. Note that different color scales are used. (For interpretation of the references to color in this figure legend, the reader is referred to the web version of this article.)

C, the subtidal components dominate the tidal components. Overall, the differences of c at the three stations fluctuate similarly to c, with a significant reduction due to the diversion. The reduction intermittently occurs with tides at Station A, most significantly during strong tidal currents (~50% relative to the normal case; Fig. 11a). At Station B, ~3.5 km from the TSTP, the level of c decreases to approximately a quarter of that at Station A; yet, the reduction by the diversion reaches ~50% (Fig. 11b). In contrast, the reduction of c at Station C occurs mostly at subtidal low frequencies. The subtidal variability dominates the tidal variability; thus, the reduction due to the diversion lasts much longer (Fig. 11c).

5.4. Effluent flux budget analysis

To quantify the impact of the sewage effluent on the seaweed farm for the two cases, we evaluated the effluent concentration flux crossing an arbitrary section with an area A_c:

$$F = \int_{A_c} cu_n dA_c, \tag{5}$$

where A_c is the cross-sectional area and u_n is the velocity normal to the considered section. Because c is dimensionless with normalization by the source concentration C_p, F has the unit $m^3\,s^{-1}$. We further introduce the cumulative tracer flux Q (m^3) by integrating F over a given elapsed period of t from $t = 0$ as follows.

$$Q(t) = \int_0^t F dt. \tag{6}$$

We show the time series of the incoming cumulative fluxes Q, denoted by Q_{farm}, across the perimeter of the seaweed farm surrounded by four cross sections (Fig. 1c) starting at 0:00 UTC on September 21 for the two cases and their difference, ΔQ_{farm}, defined as diversion – normal (Fig. 12). Because the flux budget Q_{farm} for both cases is mostly positive, the effluent released from the TSTP gradually accumulates on the farm with time. The diversion yields a lower Q_{farm} than the normal case, leading to a net reduction of the effluent, viz., $\Delta Q_{farm} < 0$ (Fig. 12b). The time-averaged Q_{farm} during the plotted period is also lower in the diversion case with $2.01 \times 10^4\,m^3$ than in the normal case with $2.83 \times 10^4\,m^3$ (the time-averaged ΔQ_{farm} is $-0.82 \times 10^4\,m^3$), as summarized in Table 3. The temporal variability in Q_{farm} and ΔQ_{farm} consists of tidal and subtidal components, where the latter contributes more than the former. An increase and subsequent decrease of Q_{farm} and

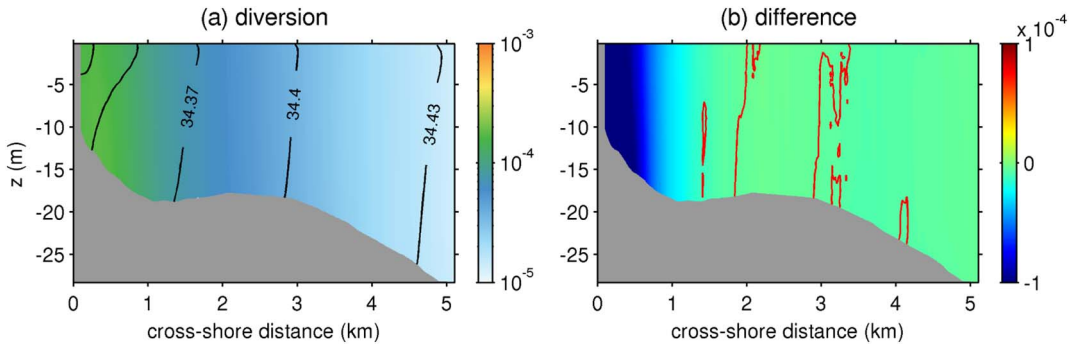

Fig. 10. Same as Fig. 9a and b but for the eastern transect (ET in Fig. 1c).

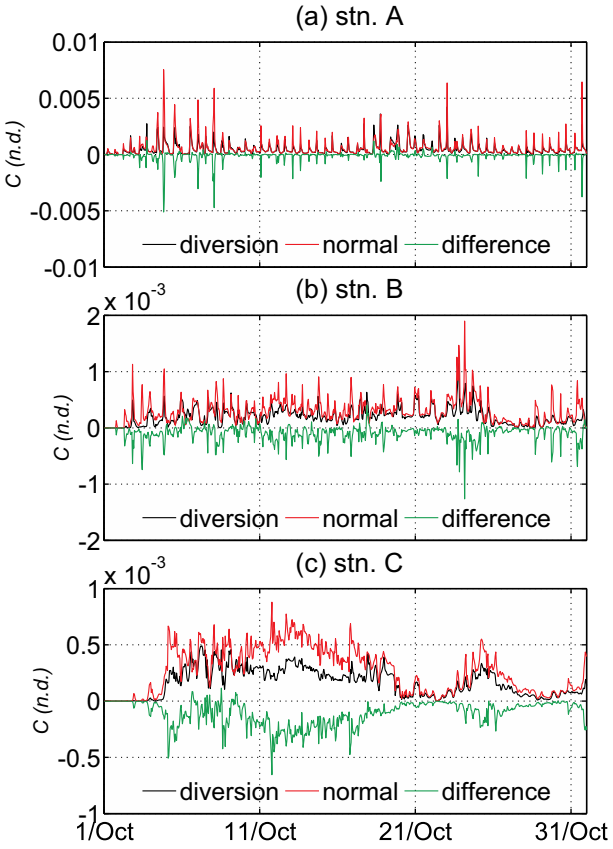

Fig. 11. Time series plots of the surface tracer concentration, c, at Stations A, B, and C (Fig. 1c). The black, red, and green lines indicate the diversion, normal, and difference (diversion - normal), respectively. (For interpretation of the references to color in this figure legend, the reader is referred to the web version of this article.)

ΔQ_{farm} occurs periodically at a period of ~14 days, consistent with a spring–neap tidal cycle, with maxima on October 3, 17, and 31. The peak Q_{farm} values are 1.84×10^4 m^3, 3.67×10^4 m^3, and 5.49×10^4 m^3 in the diversion case, while they are 3.51×10^4 m^3, 5.08×10^4 m^3, and 6.53×10^4 m^3 in the normal case, respectively (Fig. 12a). These results indicate that the diversion adequately reduces the sewage influence (by ~28% on average) on the seaweed farm. It is worth addressing that the outgoing Q at the perimeter of the L4 domain, Q_{L4}, is dominated by that from the western open boundary toward the Harima Sea due to strong tidal currents formed near the Akashi Strait (Fig. 7a), accounting for > 75% of the total outgoing Q_{L4} (not shown). The difference in Q_{L4} between the two cases is subtle because of the short distance between the normal and diversion outfalls (500 m) relative to the size of the L4 domain.

Doblin and Clayton (1995) reported that a high concentration of sewage effluent has a serious impact on the seaweed growth during its early life circle (viz., in fall). Maruyama et al. (1985) showed that the growth rate of seaweed, *Porphyra yezoensis*, is exponentially retarded due to the increased addition of sewage water under low sewage

Table 3
Cumulative nondimensional tracer fluxes in the seaweed farm, Q_{farm} (m^3).

	Until Oct. 3rd	Until Oct. 17	Until Oct. 31	Average
Diversion	1.84×10^4	3.67×10^4	5.49×10^4	2.01×10^4
Normal	3.51×10^4	5.08×10^4	6.53×10^4	2.83×10^4
Difference	-1.67×10^4	-1.41×10^4	-1.04×10^4	-0.82×10^4

Difference: diversion - normal.

concentration conditions (> 5%). This is the case for the present conditions, where the surface concentration in the farm is only 0.1%–0.01% relative to that at the source (Fig. 8a). As stated in Section 2.2, the computed far-field relative concentration of O (10^{-3}) and differences between the two cases of O (10^{-4}) are translated into the corresponding actual values by multiplying the source concentration C_p. Typical C_p may be represented by the tolerable limits of biochemical oxygen demand (BOD), nitrogen, and phosphorus contents are 160 mg/L (or 160 ppm with the daily mean of 120 mg/L), 120 mg/L (60 mg/L), and 16 mg/L (8 mg/L), respectively, as set in the wastewater standards (https://www.env.go.jp/en/focus/docs/files/20120801-51.pdf). This leads to a rough estimate of far-field concentration of 0.01–0.1 ppm, which is generally one order of magnitude higher than the detection limits (World Health Organization, 2011). The effect of the diversion, i.e., the averaged reduction of ~28%, is anticipated to be marginally favorable to the growth of the seaweed, because local seaweed farmers are generally satisfied with the fall diversion. Although the farmers claim that the TSTP overdoses the seaweed culture, they occasionally complained once in several years that the diversion would not have worked adequately. Apparently the seaweed cultures are influenced by many factors, not only by the nutrient load from the adjacent treatment plant, but also by light, turbidity, temperature, nutrients from the rivers and the offshore waters, etc. A farther detailed assessment is necessary for more comprehensive protection of the seaweed culture in the future.

Fig. 13 shows the time series of instantaneous F and cumulative Q at the four cross sections surrounding the seaweed farm. The subscripts represent the western, northern, eastern, and southern cross sections, respectively. For example, F_w denotes F at the western cross section. The sum of the four cumulative fluxes is identical to Q_{farm}. Tidal and subtidal fluctuations are manifested in all four F values; yet, their contribution differs from section to section. F_w and F_s fluctuate primarily at diurnal or semidiurnal tidal frequencies, while the lower-frequency subtidal contribution is more prominent for F_n and F_e. Nevertheless, high-frequency tidal variability of the instantaneous fluxes has a minor or even negligible contribution to the net impact of the effluent. For instance, at the western section closest to the outfall, even if a negative F_w prevails, the cumulative Q_w is positive and has an apparent increasing trend because the positive F_w lasts longer than the negative F_w (Fig. 13a and b). The cumulative Q shows an increase, except for Q_s, where the largest amount of c discharges out of the farm, which is compensated for by the incoming c at the three other sections. Therefore, the direct impact from the TSTP manifests at the western and northern sections showing the highest transport offshore (southward) and eastward, yielding the overall cross- and alongshore gradients of the surface c, as shown in Fig. 8a.

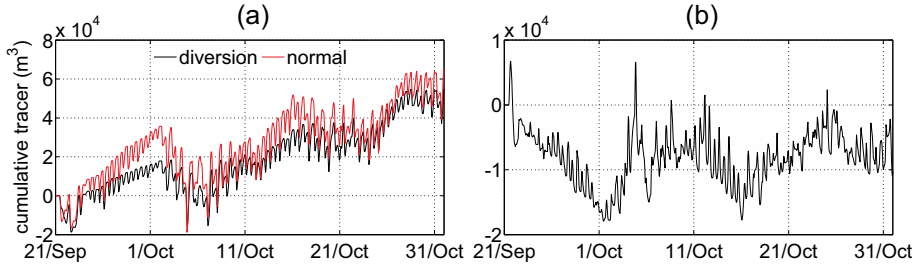

Fig. 12. (a) Time series plot of temporally cumulative net tracer fluxes stored in the seaweed farm area, Q_{farm} (m^3). The black and red curves denote the diversion and normal cases. (b) The temporal changes of the difference of Q_{farm} (m^3) for the two cases (diversion - normal). (For interpretation of the references to color in this figure legend, the reader is referred to the web version of this article.)

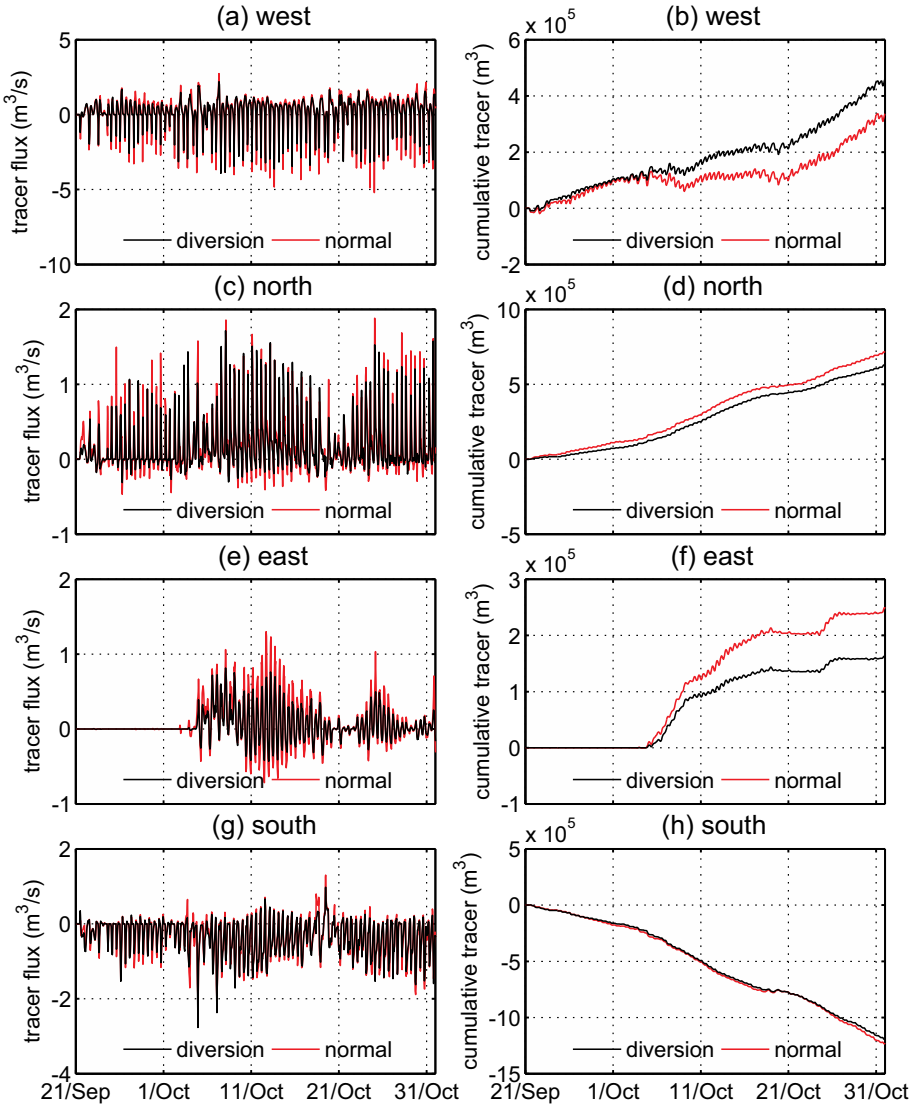

Fig. 13. Time series plot of the instantaneous tracer flux F ($m^3\,s^{-1}$, left panels) and corresponding cumulative tracer fluxes Q (m^3, right panels) at the four boundaries surrounding the seaweed farm. From top to bottom, the figures show F and Q at the western, northern, eastern, and southern transects, respectively. The black and red curves denote the values for the diversion and normal cases. (For interpretation of the references to color in this figure legend, the reader is referred to the web version of this article.)

The eastern cumulative Q_e has a remarkable time lag of ~14 days behind Q_w, Q_n, and Q_s; the effluent appears immediately after the initialization. The farm is generally affected by nearshore westward residual current (Fig. 7a) that initially carries no effluent. Tidal currents give rise to oscillatory effluent transport back and forth in the alongshore direction within the farm. Hence, the farm is more influenced near the outfall (Fig. 8a) due to the retarded initial arrival of the effluent. However, the magnitude of Q_e is smallest among the four sections. Because Q_e increases with time, the incoming flux dominates the discharging flux. This result implies that the primary source of Q_e is the recurring effluent discharged out of the farm, likely that passing through the southern section.

Although the diversion leads to an overall reduction of the effluent accumulation in the farm relative to the case with the normal outfall (Fig. 12), it is not always the case in all four sections. The diversion results in the increase of Q at the western and southern sections, while the latter contributes less to the Q budget. Accordingly, the effluent from the diversion outfall induces more notable alongshore transport in and around the farm, whereas the cross-shore, seaward transport prevails for the normal outfall. The increased Q_w of the diversion is somewhat counterintuitive to the overall reduced c in the western section (Fig. 10), with u_n being substantially unaltered (not shown). These results indicate that the highly nonlinear, subtidal, and residual variability in c and u_n and their phase relation included in the present model are inevitable to accurately and quantitatively assess the flux cu_n.

6. Conclusions

We conducted a comprehensive, detailed assessment of the impact of the diversion at the TSTP on the adjacent seaweed farm in a narrow tidal channel connecting two subbasins in the SIS, Japan. We developed a quadruple-nested, very high-resolution configuration with a horizontal grid spacing down to 20 m based on a state-of-the-art 3-D ocean model, ROMS (Shchepetkin and McWilliams, 2005, 2008). The Eulerian near-field effluent dilution model of Uchiyama et al. (2014) was employed to reproduce 3-D advection–dispersion processes of the under-resolved, bottom-released buoyant effluent plume at the TSTP.

The reproducibility of the model was first confirmed with in situ observations to ensure reasonable agreement. The time-averaged residual 3-D dynamics and their temporal variability were then extensively analyzed. The time-averaged surface currents are primarily driven by the clockwise Okinose Circulation formed off the TSTP, which

substantially determines the large-scale, residual dynamics including the nearshore counterclockwise recirculation manifested near the TSTP. The currents fluctuate prominently at semidiurnal and diurnal tidal frequencies, with a notable influence of low-frequency subtidal variability. The TSTP and western portion of the seaweed farm located closer to the tidal strait are largely affected by tidal currents. In contrast, subtidal residual currents induced by surface wind stresses and constrained by the Okinose Circulation have prevailing effects in the eastern portion of the farm. The effluent measured by non-dimensional Eulerian passive tracer concentration generally follows these circulation patterns. The effluent transport is mostly controlled by subtidal residual currents, in particular by the offshore-directed current of the nearshore counterclockwise recirculation that subsequently merges with the Okinose Circulation to promote southeastward offshore effluent transport.

A twin numerical experiment for cases with normal and western diversion outfalls enabled us to quantitatively evaluate the effect of the diversion. However, the dynamical effects due to the diversion were found to be subtle for the relatively small freshwater discharge of $1.80 \times 10^5\,m^3\,d^{-1}$. An overall reduction of the effluent affecting the farm was discovered, although the distance between the two outfalls is only 500 m in the alongshore direction. The effluent flux budget analysis revealed that the cumulative nondimensional effluent of the seaweed farm is reduced by $\sim 0.81 \times 10^4\,m^3$ on average compared with that of the normal outfall ($\sim 2.83 \times 10^4\,m^3$), exhibiting a ~28% reduction of the effluent from the TSTP by the diversion, which could lead to favorable influences on the growth of seaweeds. The farm located in the east of the TSTP encounters incoming effluent fluxes from the western, northern, and eastern cross sections, whereas outgoing flux is invoked at the southern section. The eastern positive flux lags behind the initialization, indicating the dominance of a recurring tracer that has flowed out of the farm or comes from the south.

Acknowledgements

The present research was financially supported by the City of Kobe and Japan Society for the Promotion of Science (JSPS) Grants-in-Aid for Scientific Research 15KK0207 and 15H04049 at Kobe University. The design and effluent data for the Tarumi Sewage Treatment Plant were provided by the City of Kobe.

References

Abowei, J.F.N., Ezekiel, E.N., 2013. The potentials and utilization of seaweeds. Sci. Agric. 4 (2), 58–66.
Becker, J.J., Sandwell, D.T., Smith, W.H.F., Braud, J., Binder, B., Depner, J., Fabre, D., Factor, J., Ingalls, S., Kim, S.-H., Ladner, R., Marks, K., Nelson, S., Pharaoh, A., Trimmer, R., Von Rosenberg, J., Wallace, G., Weatherall, P., 2009. Global bathymetry and elevation data at 30 Arc Seconds Resolution: SRTM30_PLUS. Mar. Geod. 32 (4), 355–371.
Bricker, J.D., Nakayama, A., 2007. Estimation of far-field horizontal and vertical turbulent diffusion coefficients from the concentration field of a wastewater plume near the Akashi Strait. Environ. Fluid Mech. 7, 1–22.
Bricker, J.D., Okabe, I., Nakayama, A., 2006. Behavior of a small pulsed river plume in a strong tidal cross-flow in the Akashi Strait. Environ. Fluid Mech. 6, 203–225.
Buijsman, M., Uchiyama, Y., McWilliams, J.C., Hill-Lindsay, C.R., 2012. Modeling semidiurnal internal tides in the Sourthern California Bight. J. Phys. Oceanogr. 42, 62–77. http://dx.doi.org/10.1175/2011JPO4597.1.
Chang, P.H., Guo, X., Takeoka, H., 2009. A numerical study of the seasonal circulation in the Seto Inland Sea, Japan. J. Oceanogr. 65, 721–736.
Doblin, M.A., Clayton, M.N., 1995. Effect of secondarily-treated sewage effluent on the early life-history stage of two species of brown macroalgae: *Hormosira banksii* and *Durvillaea potatorum*. Mar. Biol. 122, 689–698.
Egbert, G.D., Erofeeva, S.Y., 2002. Efficient inverse modeling of barotropic ocean tides. J. Atmos. Ocean. Technol. 19, 183–204.
Egbert, G.D., Bennett, A.F., Foreman, M.G.G., 1994. TOPEX/POSEIDON tides estimated using a global inverse model. J. Geophys. Res. 99, 24821–24852.
Fujiwara, T., Nakata, H., 1991. Flow characteristics governing the distribution of water and bottom quality in a semi-enclosed sea. Mar. Pollut. Bull. 23, 675–678.
Fujiwara, T., Nakata, H., Nakatsuji, K., 1994. Tidal-jet and votex-pair driving of the residual circulation in a tidal estuary. Cont. Shelf Res. 14, 1025–1038.
Guo, X., Futamura, A., Takeoka, H., 2004. Residual currents in semi-enclosed bay of the Seto Inland Sea, Japan. J. Geophys. Res. 109, C12008. http://dx.doi.org/10.1029/2003JC002203.
Hodur, R.M., 1997. The naval research laboratory's coupled ocean/atmosphere mesoscale prediction system (COAMPS). Mon. Weather Rev. 125, 1414–1430.
Honda, S., Nakayama, A., Bricker, J.D., 2007. Field survey of advection and diffusion off Tarumi Coast using GPS drifters equipped with conductivity and temperature sensors. Proc. Coast. Eng. Conf. 54, 346–350. http://dx.doi.org/10.2208/proce1989.54.346. (in Japanese with English abstract).
Imai, I., Yamaguchi, M., Hori, Y., 2006. Eutrophication and occurrences of harmful algal blooms in the Seto Inland Sea, Japan. Plankon Benthos Res. 1 (2), 71–84.
Imasato, N., 1983. A numerical experiment on water and salt exchange through the Akashi and Naruto Straits. J. Phys. Oceanogr. 13, 1526–1533.
Imasato, N., Fujo, S., Zhang, Q., Awaji, T., Akitomo, K., 1994. Three-dimensional numerical experiments on tidal exchange through a narrow strait in a homogeneous and a stratified sea. J. Oceanogr. 50, 119–139.
Isoguchi, O., Shimada, M., Kawamura, H., 2010. Characteristics of ocean surface winds in the lee of an isolated island observed by synthetic aperture radar. Mon. Weather Rev. 139, 1744–1761.
Kamidaira, Y., Uchiyama, Y., Mitarai, S., 2017. Eddy-induced transport of the Kuroshio warm water around the Ryukyu Islands in the East China Sea. Cont. Shelf Res. 143, 206–218. http://dx.doi.org/10.1016/j.csr.2016.07.004.
Kawabe, M., 1987. Spectral properties of sea level and time scale of Kuroshio path variations. J. Oceanogr. Soc. Jpn 43, 111–123.
Kawabe, M., 1995. Variations of current path, velocity, and volume transport of the Kuroshio in relation with the large meander. J. Phys. Oceanogr. 25, 3103–3117.
Kobayashi, S., Hashimoto, E., Hagao, M., Tokasugi, Y., 2009. Variations in turbulent energy dissipation and water column stratification at the entrance of a tidally energetic strait. J. Oceanogr. 65, 657–664.
Kosako, T., Uchiyama, Y., Mitarai, S., 2016. A multi-year analysis on circulation and associated larval transport in the Seto Inland Sea, Japan. J. Jpn Soc. Civil Eng. Ser. B2 72 (2), 1273–1278. http://dx.doi.org/10.2208/kaigan.72.I_1273. (in Japanese with English abstract).
Kurosawa, K., Uchiyama, Y., Miyoshi, Y., 2017. On improvement of an estuarine reanalysis-forecast model for the Seto Inland Sea based on 3D variational assimilation. J. Jpn Soc. Civil Eng. Ser. B2 73 (2), 1663–1668 (in Japanese with English abstract).
Li, Y., Wolanski, E., Zhang, H., 2015. What processes control the net currents through shallow straits? A review with application to the Bohai Strait, China. Estuar. Coast. Shelf Sci. 158, 1–11.
Maruyama, T., Miura, A., Yoshida, T., 1985. The effects of effluent of municipal wastewater on the growth of *Porphyra yezoensis* in the case of static culture. Bull. Jpn. Soc. Sci. Fish. 51 (2), 315–320 (in Japanese with English abstract).
Mason, E., Molemake, J., Shchepetkin, A.F., Colas, F., McWilliams, J.C., Sangrà, P., 2010. Procedures for offline grid nesting in regional ocean models. Ocean Model. 35, 1–15.
Miller, T.W., Omori, K., Hamaoka, H., Shibata, J., Hidejiro, O., 2010. Tracing anthropogenic inputs to production in the Seto Inland Sea, Japan – a stable isotope approach. Mar. Pollut. Bull. 60, 1803–1809.
Mishima, Y., Hoshika, A., Tanimoto, T., 1999. Deposition rates of terrestrial and marine organic carbon in the Osaka Bay, Seto Inland Sea, Japan, determined using carbon and nitrogen stable isotope rations in the sediment. J. Oceanogr. 55, 1–11.
Miyazawa, Y., Zhang, R., Guo, X., Tamura, H., Ambe, D., Lee, J., Okuno, A., Yoshinari, H., Setou, T., Komatsu, K., 2009. Water mass variability in the western North Pacific detected in 15-year eddy resolving ocean reanalysis. J. Oceanogr. 65, 737–756.
Nakatsuji, K., Fujiwara, T., Kurita, H., 1994. An estuarine system in semi-enclosed Osaka Bay in Japan. In: Dyer, K.R., Orth, R.J. (Eds.), Changes in Fluxes in Estuaries: Implications From Science to Management, ECSA22/EFR Symposium. Olsen & Olsen, Fredensborg, Denmark, pp. 79–84.
Nakayama, A., Nizamani, Z., 2016. Simulation of near field mixing process in marine disposal of treated sewer water. J. Eng. Appl. Sci. 11 (4), 2205–2210 (ISSN 1819-6608).
Niwa, K., Aguga, Y., 2006. Identification of currently cultivated Porphyra species by PCR-RFLP analysis. Fish. Sci. 72, 143–148.
Rodriguez, E., Morris, J.E., Belz, J.E., Chapin, E.C., Martin, J.M., Daffer, W., Hensley, S., 2005. An Assessment of the SRTM Topographic Products. Technical Report. Jet Propulsion Laboratory, Pasadena, CA.
Rodriguez, E., Morris, C.S., Belz, J.E., 2006. A global assessment of the SRTM performance. Photogramm. Eng. Remote. Sens. 72 (3), 249–260. http://dx.doi.org/10.14358/PERS.72.3.249.
Romero, L., Uchiyama, Y., Ohlmann, C., McWilliams, J.C., Siegel, D.A., 2013. Simulation od particle-pair dispersion in the Southern California coastal zone. J. Phys. Oceanogr. 43, 1862–1879. http://dx.doi.org/10.1175/JPO-D-13-011.1.
Shchepetkin, A.F., McWilliams, J.C., 2005. The regional ocean modeling system (ROMS): a split-explicit, free-surface, topography-following-coordinate oceanic model. Ocean Model. 9, 347–404.
Shchepetkin, A.F., McWilliams, J.C., 2008. Computational kernel algorithms for fine-scale, multiprocess, longtime oceanic simulations. In: Temam, R., Tribbia, J. (Eds.), Handbook of Numerical analysis: Computational Methods for the Ocean and the Atmosphere. Elsevier, Amsterdam, pp. 119–181.
Tada, H., Uchiyama, Y., Masunaga, E., 2017. Impacts of two super typhoons on the Kuroshio and marginal seas off the Pacific coast of Japan. Deep Sea Res., Part I 132, 80–93. http://dx.doi.org/10.1016/j.dsr.2017.12.007.
Takeoka, H., 2002. Progress in Seto Inland Sea research. J. Oceanogr. 58, 93–107.
Takeoka, H., Akiyama, H., Kikuchi, T., 1993. The Kyucho in the Bungo Channel, Japan-Periodic intrusion of oceanic warm water. J. Oceanogr. 49, 369–382.
Terawaki, T., Yoshikawa, K., Yoshida, G., Uchimura, M., Iseki, K., 2003. Ecology and restoration techniques for Sargassum beds in the Seto Inland Sea, Japan. Mar. Pollut. Bull. 47, 198–201.

Tomita, A., Nakura, Y., Ishikawa, T., 2016. New direction for environmental water management. Mar. Pollut. Bull. 102, 323–328.
Tsuge, T., Washida, T., 2003. Economic valuation of the Seto Inland Sea by using an Internet CV survey. Mar. Pollut. Bull. 47, 230–236.
Tsujimoto, A., Nomura, R., Yasuhara, M., Yamazaki, H., Yoshikawa, S., 2006. Impact of eutrophication on shallow marine benthic foraminifers over the last 150 years in Osaka Bay, Japan. Mar. Micropaleontol. 60, 258–268.
Uchiyama, Y., McWilliams, J.C., Shchepetkin, A.F., 2010. Wave-current interaction in an oceanic circulation model with a vortex force formalism: application to the surf zone. Ocean Model. 34 (1–2), 16–35. http://dx.doi.org/10.1016/j.ocemod.2010.04.002.
Uchiyama, Y., Idica, E.Y., McWilliams, J.C., Stolzenbach, K.D., 2014. Wastewater effluent dispersal in Southern California Bays. Cont. Shelf Res. 76, 36–52. http://dx.doi.org/10.1016/j.csr.2014.01.002.
Uchiyama, Y., Suzue, Y., Yamazaki, H., 2017a. Eddy-driven nutrient transport and associated upper-ocean primary production along the Kuroshio. J. Geophys. Res. Oceans 122, 5046–5062. http://dx.doi.org/10.1002/2017JC012847.
Uchiyama, Y., Kanki, R., Takano, A., Yamazaki, H., Miyazawa, Y., 2017b. Mesoscale reproducibility in regional ocean modeling with a 3-D stratification estimate based on Aviso-Argo data. Atmosphere-Ocean 55, 1–18. http://dx.doi.org/10.1080/07055900.2017.1399858.
Uchiyama, Y., McWilliams, J.C., Akan, C., 2017c. Three-dimensional transient rip currents: bathymetric excitation of low-frequency intrinsic variability. J. Geophys. Res. Oceans 122, 5826–5849. http://dx.doi.org/10.1002/2017JC013005.
Woodruff, S.D., Slutz, R.J., Jenne, R.L., Steurer, P.M., 1987. A comprehensive ocean-atmosphere data set. Bull. Am. Meteorol. Soc. 68, 1239–1250.
World Health Organization, 2011. Nitrate and Nitrite in Drinking-water: Background document for development of WHO Guidelines for Drinking-water Quality, Rev. 1, Geneva, Switzerland. (23 p).